NASA/TM—2019-220212 AIAA–2019–2642



One-Third-Octave Analysis of Core/Combustor-Noise Measurements for the DGEN Aeropropulsion Research Turbofan With Application to Noise Prediction

Lennart S. Hultgren, Devin K. Boyle, and Brenda S. Henderson
Glenn Research Center, Cleveland, Ohio

May 2019

NASA STI Program . . . in Profile

Since its founding, NASA has been dedicated to the advancement of aeronautics and space science. The NASA Scientific and Technical Information (STI) Program plays a key part in helping NASA maintain this important role.

The NASA STI Program operates under the auspices of the Agency Chief Information Officer. It collects, organizes, provides for archiving, and disseminates NASA's STI. The NASA STI Program provides access to the NASA Technical Report Server—Registered (NTRS Reg) and NASA Technical Report Server—Public (NTRS) thus providing one of the largest collections of aeronautical and space science STI in the world. Results are published in both non-NASA channels and by NASA in the NASA STI Report Series, which includes the following report types:

- TECHNICAL PUBLICATION. Reports of completed research or a major significant phase of research that present the results of NASA programs and include extensive data or theoretical analysis. Includes compilations of significant scientific and technical data and information deemed to be of continuing reference value. NASA counter-part of peer-reviewed formal professional papers, but has less stringent limitations on manuscript length and extent of graphic presentations.

- TECHNICAL MEMORANDUM. Scientific and technical findings that are preliminary or of specialized interest, e.g., "quick-release" reports, working papers, and bibliographies that contain minimal annotation. Does not contain extensive analysis.

- CONTRACTOR REPORT. Scientific and technical findings by NASA-sponsored contractors and grantees.

- CONFERENCE PUBLICATION. Collected papers from scientific and technical conferences, symposia, seminars, or other meetings sponsored or co-sponsored by NASA.

- SPECIAL PUBLICATION. Scientific, technical, or historical information from NASA programs, projects, and missions, often concerned with subjects having substantial public interest.

- TECHNICAL TRANSLATION. English-language translations of foreign scientific and technical material pertinent to NASA's mission.

For more information about the NASA STI program, see the following:

- Access the NASA STI program home page at http://www.sti.nasa.gov

- E-mail your question to help@sti.nasa.gov

- Fax your question to the NASA STI Information Desk at 757-864-6500

- Telephone the NASA STI Information Desk at 757-864-9658

- Write to:
  NASA STI Program
  Mail Stop 148
  NASA Langley Research Center
  Hampton, VA 23681-2199

NASA/TM—2019-220212 AIAA–2019–2642



One-Third-Octave Analysis of Core/Combustor-Noise Measurements for the DGEN Aeropropulsion Research Turbofan With Application to Noise Prediction

Lennart S. Hultgren, Devin K. Boyle, and Brenda S. Henderson
Glenn Research Center, Cleveland, Ohio

Prepared for the
25th AIAA/CEAS Aeroacoustics Conference
cosponsored by the American Institute of Aeronautics and Astronautics (AIAA) and
Council of European Aerospace Societies (CEAS)
Delft, The Netherlands, May 20–23, 2019

National Aeronautics and
Space Administration

Glenn Research Center
Cleveland, Ohio 44135

May 2019

Acknowledgments

This work was sponsored by the Advanced Air Vehicles Program, Advanced Air Transport Technology Project, under the Aircraft Noise Reduction Subproject at the NASA Glenn Research Center. The Aero-Acoustic Propulsion Laboratory (AAPL) staff are thanked for their expertise and dedication in preparing and executing the 2017 test campaign.

This work was sponsored by the Advanced Air Vehicle Program
at the NASA Glenn Research Center

Trade names and trademarks are used in this report for identification only. Their usage does not constitute an official endorsement, either expressed or implied, by the National Aeronautics and Space Administration.

Level of Review: This material has been technically reviewed by technical management.

Available from

NASA STI Program
Mail Stop 148
NASA Langley Research Center
Hampton, VA 23681-2199

National Technical Information Service
5285 Port Royal Road
Springfield, VA 22161
703-605-6000

This report is available in electronic form at http://www.sti.nasa.gov/ and http://ntrs.nasa.gov/

One-Third-Octave Analysis of Core/Combustor-Noise Measurements for the DGEN Aeropropulsion Research Turbofan With Application to Noise Prediction

Lennart S. Hultgren, Devin K. Boyle, and Brenda S. Henderson
National Aeronautics and Space Administration
Glenn Research Center
Cleveland, Ohio 44135

Abstract

This work continues the analysis of data obtained during a 2017 NASA DGEN Aeropropulsion Research Turbofan (DART) core/combustor-noise baseline test in the NASA GRC Aero-Acoustic Propulsion Laboratory (AAPL). The DART is a cost-efficient testbed for the study of core-noise physics and mitigation. Acoustic data were simultaneously acquired using the AAPL overhead microphone array in the engine aft-quadrant farfield, a single midfield microphone, and two infinite-tube-probe sensors for unsteady pressures at the core-nozzle exit. The data are here examined on an 1/3-octave basis as a first step in extending and improving core-noise prediction capability.

I. Introduction

In order to study propulsion-noise production, propagation, diagnostics and, particularly, mitigation in a relevant environment, NASA acquired a Price Induction DGEN 380 turbofan engine in 2017. The DGEN 380 is a two-spool 500 lbf (2.2 kN) thrust-class geared turbofan engine with a bypass ratio of approximately 7.6, a 3.32 fan gear ratio, a single centrifugal compressor on the high pressure spool, a reverse-flow annular combustor, and single-stage uncooled axial high-pressure and low-pressure turbines. It is intended for twin-jet applications in the nascent very-light-jet (VLJ), or personal-light-jet, market [1]. Even though it is a rather small turbofan engine, its acoustic signature is relevant to large commercial aircraft engines [2–4]. This NASA resource has been designated as the DGEN Aero-Propulsion Research Turbofan (DART). It promises to be a cost-effective research platform since major components can be replaced with parts modified for invasive instrumentation with comparative ease, due to the DGEN 380 modular design, and operating costs are expected to be relatively low because of its size.

NASA has carried out two DGEN 380 core-noise tests [2, 4]. First, a limited test was carried out during 2014 to evaluate the feasibility of the (then) DART concept as a propulsion acoustics testbed [2, 3]. In this test a DGEN 380 turbofan engine mounted on the back of a small flatbed truck was placed in the anechoic Aero-Acoustic Propulsion Laboratory (AAPL) at NASA Glenn Research Center (GRC). Among several objectives, one particular interest [2] was to establish how well the DGEN 380's core/combustor-noise characteristics relate to those of current-generation combustors used in turbofan engines larger than the comparatively small DGEN 380. Data were acquired simultaneously from a core-exhaust-mounted infinite-tube probe (ITP) for pressure and a midfield microphone arc array. The array had a constant radius of 12 ft (3.7 m), measured from the engine exit, fixed azimuthal angle, and was located at the engine centerline height. Farfield microphone data were also acquired [3] during this test, but not synchronously with the ITP and midfield-array data, and therefore were of limited use from a core-noise point of view. A well-established two-signal source-separation technique [5, Ch. 4] was used to educe the low-frequency broadband combustor-noise component of the total noise signature at the midfield-array location in the 130° polar direction (engine-aft quadrant). The results indicated [2] that the DART concept would be a relevant and valuable asset for studying core-noise physics and evaluating novel-measurement and noise-mitigation techniques. Hultgren [2] also compared the combustor-noise results with predictions obtained by using the NASA Aircraft Noise Prediction Program (ANOPP) [6, 7] and proposed a thrust-class correction for the predictions. After applying this operation-independent correction, the predictions agreed well with data for all the engine-power conditions of the test.

Second, a baseline core/combustor-noise test [4] using the DART in the AAPL was performed during August 2017. In a sense, this was an extensive repeat of the limited 2014 test, with improved instrumentation and simultaneous acoustic data also acquired in the acoustic/geometric farfield. The test purpose was to establish a baseline dataset for

future core/combustor-noise measurements using the DART and to compare with results obtained during the 2014 feasibility test using a different DGEN 380 turbofan. The narrowband acoustic results and findings from this test are reported by Boyle et al. [4].

The purpose of the present work is to further analyze the data from the 2017 baseline test, but now on an 1/3-octave basis, in order to further examine the suggested [2] VLJ thrust-class correction to the semi-empirical model for combustor-noise prediction in the ANOPP-module GECOR, as well as as ultimately extending and improving (ANOPP) core-noise prediction capability.

II. Experimental Setup

The setup, instrumentation, engine control, and test conditions for the 2017 DART core/combustor-noise baseline test are described in detail in Boyle et al. [4]. Consequently, only a brief summary of the most relevant details is given here. The turbofan engine was located near the center of the AAPL allowing use of the fixed overhead farfield microphone array. The coordinate system used to describe measurement locations is a spherical one with its origin located on the engine centerline at the core-nozzle exit plane. The polar angle is zero in the inlet direction and the azimuthal angle is zero in the engine port-side (left-hand side facing forward) horizontal plane.

A. Instrumentation Layout

Seven of the existing 24 microphone locations of the AAPL overhead array were utilized in this test. The microphones were oriented such that their faces pointed at the center of the core-exhaust plane. The microphone layout is described in Table 1. The overhead-array microphones are labeled as sensors FF017 through FF023, with the 'FF' indicating

Table 1 Microphone locations in spherical coordinates

	FF017	FF018	FF019	FF020	FF021	FF022	FF023	MF101
radius, ft	39.56	38.81	38.25	37.55	37.05	36.63	36.57	10.0
(m)	(12.06)	(11.83)	(11.66)	(11.44)	(11.29)	(11.16)	(11.15)	(3.05)
polar, °	108.04	113.48	119.22	125.18	131.21	137.22	143.35	130.00
azimuth, °	83.04	83.02	82.98	83.05	83.95	84.74	87.20	0

farfield and the numerical part increasing with aft position. The azimuthal angles of the overhead-array microphones were nearly constant at 83° with a slight variation due to the out-of-azimuthal-plane rotation of the array. The polar angles fall in the approximate range of 108° to 143° at radial distances from the engine core exit of about 36–39 ft (11–12 m). The overhead microphones can be considered to be in the geometric farfield, according to the criteria given by Ahuja [8], since the mean distance between the overhead-array measurement locations and the core-nozzle exit is approximately 51 nozzle diameters. In addition to the microphones mounted in the aft portion of the overhead array, a single (identical) midfield microphone was placed at a radial distance of 10 ft (3.05 m), at the engine centerline height and at a polar angle of 130°. It is labeled as sensor MF101, with the 'MF' indicating midfield, in Table 1.

Two ITPs, instrumented with 10 psi (68.95 kPa) differential unsteady pressure transducers, were also installed at the core-nozzle exit providing engine-internal measurements. Figure 1(a) shows the location of the ITPs in more detail. The ITPs at the the 6 o'clock and 7 o'clock positions are herein referred to as sensors NE801 and NE802, respectively, with the 'NE' indicating (core) nozzle exit. The ITP design is indicated in Fig. 1(b).

B. Test Points

The campaign consisted of the test points shown in Table 2. The power setting represents the ratio of temperature-corrected low-pressure-shaft speed

$$N_{\mathrm{Lc}} = N_{\mathrm{L}}\sqrt{T_{\mathrm{SLS}}/T_{\mathrm{amb}}} \tag{1}$$

where N_{L} is the actual shaft speed, $T_{\mathrm{SLS}} = 288.15$ K is the sea-level standard temperature, and T_{amb} is the ambient temperature (also in K) during a test point, to the maximum allowable low-pressure-shaft speed at standard sea-level conditions. The full authority digital engine control (FADEC) unit of DART has an executable program that runs through this sequence of predefined engine power settings, with each setting here set to be held for 120 seconds. The control program starts at idle (33%) and dwells at each of the power settings shown in Table 2. After having reached the maximum available power setting (limited by the ambient temperature), it then returns to idle, and the sequence is

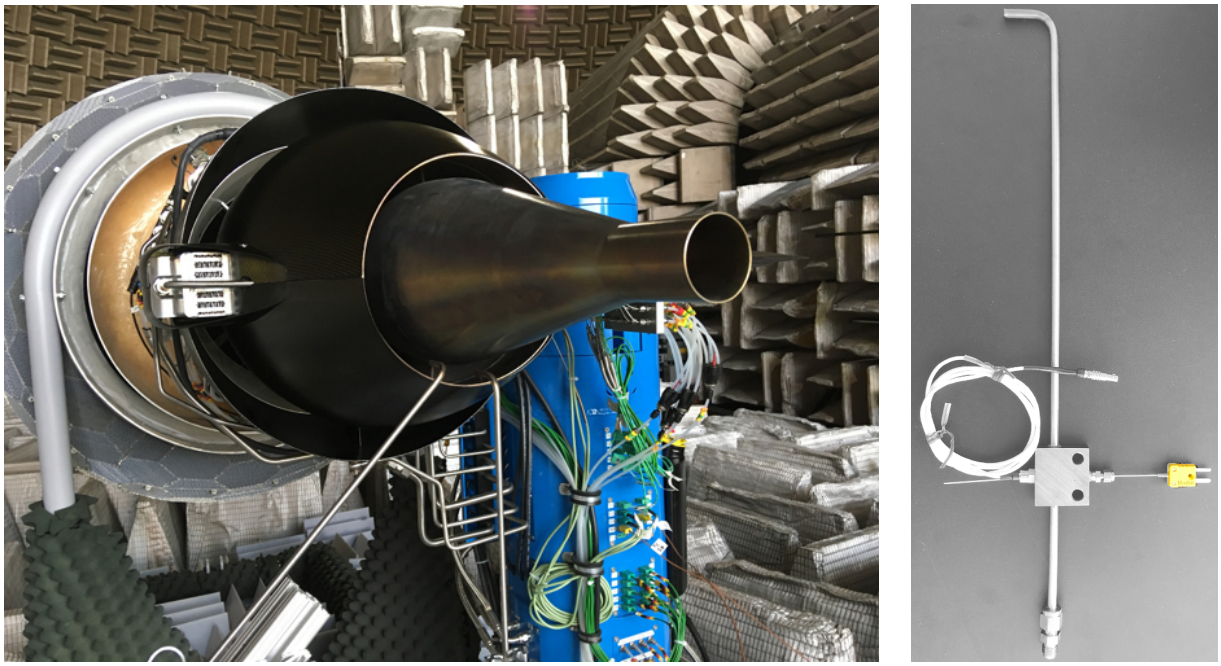


Fig. 1 (a) 6 o'clock (NE801) and 7 o'clock (NE802) ITPs at DART core-nozzle exit; (b) ITP design—sense line (top), connector to infinite line (bottom), thermocouple (right), and differential pressure transducer (left)

then repeated once. Consequently, data were collected four times at the idle set point and twice at each of the other engine-power set points. Note that the maximum-power set point depends on the ambient temperature and this is why the engine power differs slightly between test point 8 and 16. Test point 17 was taken with the engine off but with support systems (such as the oil pump, etc.) running for a background-noise assessment. Under FADEC command, the engine performed quite repeatably in maintaining shaft speed for a given set point. The actual low-speed-shaft rotation rate, N_{L}, had an *rms* deviation of less than 0.04% and its maximum observed deviation was less than 0.1%.

Table 2 DART core/combustor-noise baseline test matrix

Test Point	1	2	3	4	5	6	7	8	9	10	11	12	13	14	15	16	17
Power, %	33	33	50	60	70	80	90	92.5	33	33	50	60	70	80	90	92.3	0

Based on data reported by the FADEC, Boyle et al. [4] computed shaft-passing frequencies for the high-pressure spool, SPF_{H}, low-pressure spool, SPF_{L}, and the fan shaft, SPF_{F}, as well as blade-passing frequencies for the fan, BPF_{F}, and low-pressure turbine, BPF_{L}, corresponding to these test points. For convenience, these results [4] are reproduced in Table 3. Many of the tones were apparent either in the narrowband sound-pressure-level (*SPL*) spectra or in the 2-signal coherence spectra computed by Boyle et al. [4]. Note that the BPF_{L} tone only fell within the 10 kHz limit of their narrowband spectra for the idle power settings.

C. Data Acquisition and General Processing

The eight microphone signals and the two ITP signals were simultaneously digitized at 100,000 samples per second during a total observation time of 60 seconds at each experimental test point. Each individual time series thus contains 6 million data points. In general, narrowband auto-spectra and cross-spectra were computed [4] using an FFT length of 16,384 points (corresponding approximately to a 6.1 Hz frequency resolution or binwidth), Hamming windowing, and a 50 percent data-segment overlap. The resulting narrowband spectra are the average of a large number of realizations (over 700 instantaneous spectra). Auto-spectra were computed using both the built-in capabilities of the National Instruments™ LabVIEW software that was used to control the data acquisition and post-test using MATLAB scripts and routines. Cross-spectra were computed using MATLAB with time-of-flight corrections applied to the microphone signals when appropriate. In this paper, the narrowband results are converted to produce 1/3-octave *SPL* results.

Table 3 Low/high-pressure-spool and fan shaft frequencies and fan/low-pressure-turbine blade-passing frequencies [4]

Point #	Power, %	SPF_H, Hz	SPF_L, Hz	SPF_F, Hz	BPF_L, Hz	BPF_F, Hz
1	33	452	244	73	9253	1027
2	33	453	244	73	9256	1027
3	50	611	370	112	14069	1561
4	60	681	444	134	16884	1874
5	70	739	518	156	19701	2186
6	80	787	593	179	22518	2499
7	90	831	667	201	25332	2811
8	92.5	842	685	206	26022	2888
9	33	454	244	73	9255	1027
10	33	453	244	73	9256	1027
11	50	612	370	112	14074	1562
12	60	682	445	134	16890	1874
13	70	739	519	156	19707	2187
14	80	787	593	179	22521	2499
15	90	831	667	201	25337	2812
16	92.3	842	684	206	26002	2885

III. ANOPP GECOR 1/3-Octave Combustor-Noise Models

Combustor-noise prediction in NASA ANOPP [6, 7] is provided by the GECOR subroutine. This module essentially contains two basic semi-empirical models with options. The first model is fully 1/3-octave based and in its original implementation [9, 10] is customarily referred to as the SAE method. This method also contains a small-engine revision [11] (referred to as SmE herein) as well as an option for an alternate turbine-transmission-loss formula [12–16]. The second class of models, that will not be further discussed, or utilized here, has an intermediate-narrowband formulation [17] in order to account for tail-pipe resonances.

A characteristic feature of most models for combustor noise is that the farfield directivity and spectral distribution are decoupled. This is the case for both the SAE and SmE methods in ANOPP GECOR. For a static-engine test, the (dimensional) combustor-noise mean-square pressure in each 1/3-octave band (b) is given by

$$< p^2 >^{(b)} = \frac{\rho_o c_o \Pi D(\theta) S(f_b)}{4\pi r_o^2}, \tag{2a}$$

in the absence of atmospheric attenuation, where r_o is the distance between the source and the observer and ρ_o and c_o are the ambient density and speed of sound at the observer location. Π is the total radiated acoustic power by the source. $D(\theta)$ is a directivity function that depends only on the polar angle θ and satisfies the normalization condition

$$\int_0^\pi D(\theta) \sin\theta \mathrm{d}\theta = 2\,. \tag{2b}$$

$S(f_b)$ is a spectrum function satisfying

$$\sum_b S(f_b) = 1 \tag{2c}$$

and f_b is the 1/3-octave-band center frequency. Note that the total radiated acoustic power at the distance r_o from the source is given by

$$\int_A \frac{\sum_b < p^2 >^{(b)}}{\rho c} \mathrm{d}A = \Pi\,, \tag{2d}$$

where $\mathrm{d}A = r_o^2 \sin\theta \mathrm{d}\theta \mathrm{d}\phi$, with ϕ denoting the azimuthal angle. That is, in the absence of atmospheric attenuation, the total radiated acoustic power Π is preserved as the acoustic waves propagate towards the observer.

The sound pressure level $SPL^{(b)}$ in an 1/3-octave frequency band, the overall sound pressure level $OASPL$, and the overall power level $OAPWL$ are given by

$$SPL^{(b)} = 10\log(< p^2 >^{(b)} / p_{ref}^2), \tag{3a}$$

$$OASPL = 10\log(\textstyle\sum_b < p^2 >^{(b)} / p_{ref}^2) = 10\log[\rho_o c_o \Pi D(\theta)/4\pi r_o^2 p_{ref}^2], \tag{3b}$$

$$OAPWL = 10\log(\Pi/\Pi_{ref}), \tag{3c}$$

where $p_{ref} = 2 \times 10^{-5}$ Pa and $\Pi_{ref} = 1 \times 10^{-12}$ W if SI units are used. The ANOPP GECOR formula for the total acoustic power emitted by the source is

$$\Pi = 10^{K/10} c_\infty^2 \dot{m}_{core} \left(\frac{T_{t,ce} - T_{t,ci}}{T_{t,ci}}\right)^2 \left(\frac{P_{t,ci}}{P_\infty}\right)^2 \times F_{TA}, \tag{4a}$$

where the constant $K = -60.53\ldots$ in the SAE method and $K = -64.53\ldots$ in the SmE method. $\dot{m}_{core}$ is the mass flow rate into the combustor, $T_{t,ci}$ and $T_{t,ce}$ are the total temperature at the combustor inlet and exit, and $P_{t,ci}$ is the total combustor-inlet pressure. c_∞ and P_∞ are the ambient speed of sound and (static) pressure at the source location. *Note that the only difference between the SAE and SmE methods is the value of the constant K leading to a 4 dB difference in the acoustic power level!*

The factor F_{TA} in Eq. (4a) accounts for turbine attenuation, or loss, and, in the original formulation [18], is given by

$$F_{TA} = \left(\frac{\Delta T_{des}}{T_\infty}\right)^{-4}, \tag{4b}$$

where ΔT_{des} is the design-point total temperature drop across the turbine[a] and T_∞ is the reference temperature, i.e. the ambient (static) temperature at the source location. Note that the acoustic transmission loss is independent of the engine operating condition with this formulation. The GECOR module recently has been updated to also have an option to use an alternative turbine-transmission-loss formula, namely the simplified [14] Pratt & Whitney [12, 13] acoustic-turbine-loss formula,

$$F_{TA} = \frac{0.8\zeta}{(1+\zeta)^2}, \tag{4c}$$

where ζ is the ratio of the characteristic impedances across the turbine, i.e. $\zeta = \rho_{te} c_{te}/\rho_{ti} c_{ti}$ with ρ and c denoting density and speed of sound, respectively, and the subscripts 'te' and 'ti' indicating turbine exit and inlet. With this formulation, the turbine acoustic transmission loss depends on the engine operation conditions since the impedance ratio does. Hultgren [15][b] found that predictions using this formula compared well with data for flight idle, approach, cutback, and takeoff power settings from a full-scale static-engine test [19]. Eqs. (4b) and (4c) will be referred to as the GE and PW turbine-transmission-loss formulas, respectively. Note that both these loss formulas are frequency independent.

In this work, Eqs. (4a) and (4c) are used for the ANOPP predictions corresponding to the test points in Table 2. The DGEN 380 turbofan FADEC provided the relevant performance data during the testing such that the needed ANOPP-GECOR input parameters could be determined, see Appendix A for details.

IV. Results

Narrowband results from the 2017 DART core/combustor-noise baseline test are discussed in some detail in Boyle et al. [4]. The aim of this work is to examine the combustor-noise results on an 1/3-octave basis as a step towards the ultimate purpose of improving (ANOPP) core-noise prediction capability. To this end, narrowband results are summed up to yield 1/3-octave *SPL* results. Sufficient care must be taken to remove tones from the narrowband core-noise data before summation since the combustor noise is a broadband component.

A. Core/Combustor-Noise Component Identification

As in Boyle et al.. [4], determination of the core-noise component of the total noise signature is achieved through the two-signal coherence method [5, Ch. 4], also known as the coherent output method. The use of this method involves the one-sided cross power spectrum, G_{xy}, between two signals measured at different locations, x and y, and the one-sided auto spectrum of each signal, G_{xx} and G_{yy}. The magnitude-squared coherence is given by

$$\gamma_{xy}^2 = \frac{|G_{xy}|^2}{G_{xx} G_{yy}}, \tag{5}$$

[a] If this value is not available, the corresponding takeoff value can be used.

[b] Due to a typographical error, Eq. 13 in Hultgren [15] corresponding to Eq. (4c) here is inverted, but the computations therein are correct.

where all of the quantities involved can be calculated from the recorded total noise signature data at the given locations. The coherent output method then provides the estimate

$$G_{vv} = \gamma_{xy}^2 G_{yy} \tag{6}$$

for the component G_{vv} of the total measured spectra, G_{yy}, at a location of interest that is coherent with a signal at the other measurement location.

Coherence, by definition (and in theory), ranges between zero and unity, where perfect coherence exists at the latter value. Perfect coherence implies a direct linear dependence of one signal on the other. A nonzero coherence value implies the dependence of both signals on a common source in the presence of other unrelated signals at both locations. A zero value implies that the two signals are independent. In practice, where the time series are always finite, a zero coherence value will not be achieved even for perfectly unrelated signals. A statistical estimate is then used to judge if the signals are uncorrelated. Any computed coherence value lower than this limit is not significant and the two signals are considered as fully independent. A 95% confidence level will be used for this estimate herein.

B. Combustor-Noise 1/3-Octave *SPL* Results

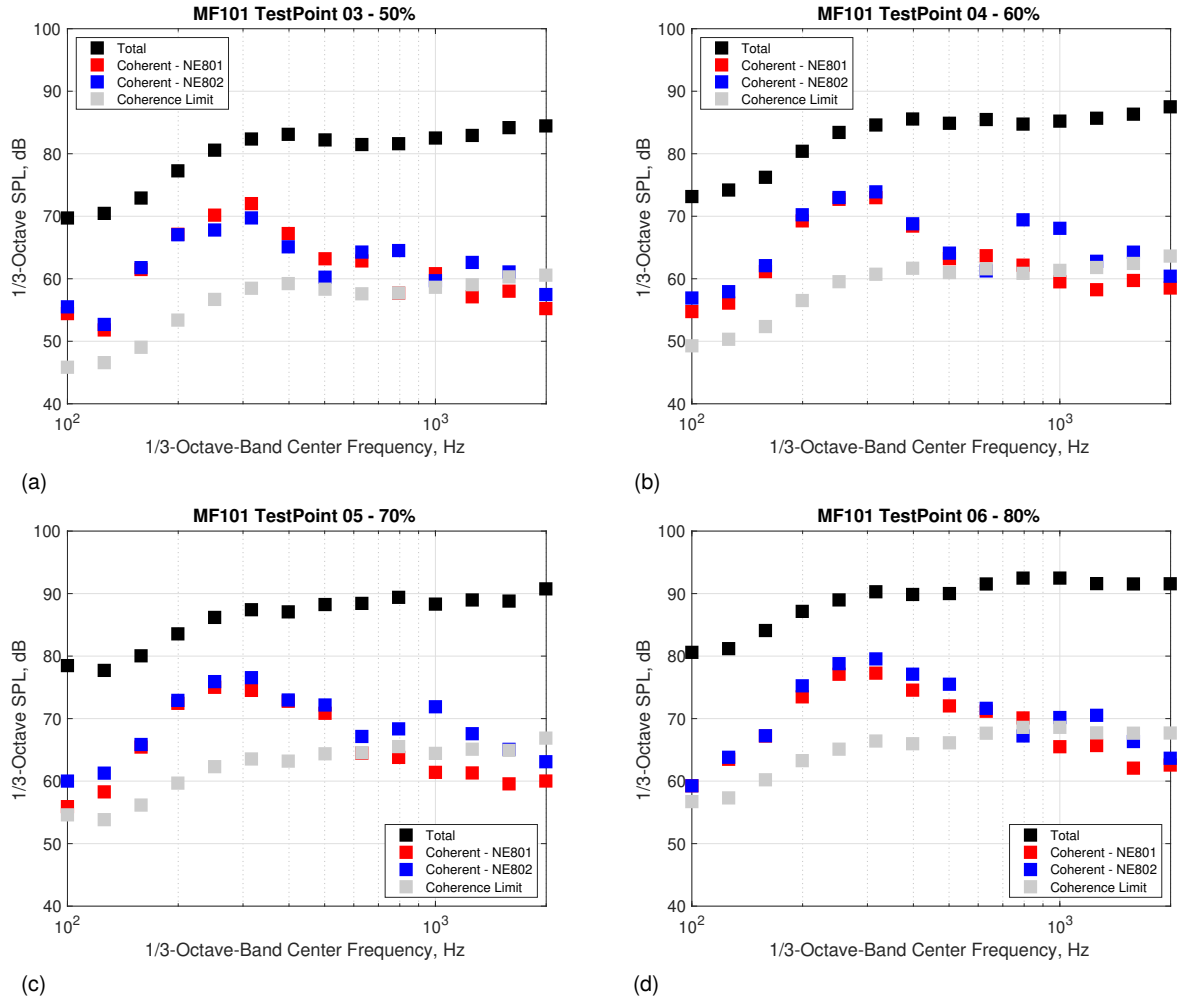


Fig. 2 Total and combustor-noise midfield 1/3-octave *SPL* in the 130^o-direction versus 1/3-octave-band center frequency; (a)–(d): black symbols—total noise signature measured by sensor MF101; red symbols—combustor-noise component using reference sensor NE801; blue symbols—combustor-noise component using reference sensor NE802; and gray symbols—coherence floor; engine power: (a) 50%, (b) 60%, (c) 70%, (d) 80%

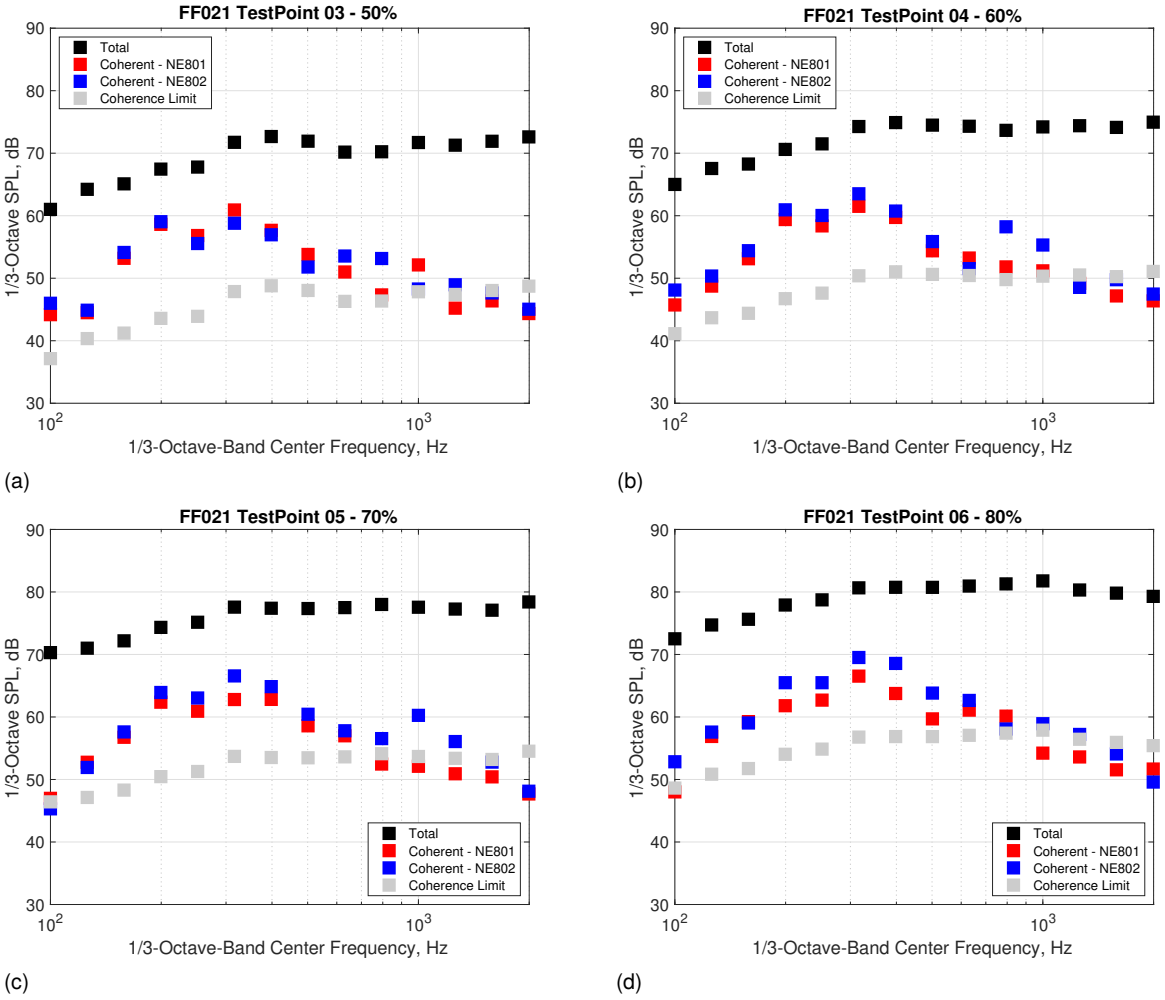


Fig. 3 Total and combustor-noise farfield 1/3-octave *SPL* in the 130^o-direction versus 1/3-octave-band center frequency; (a)–(d): black symbols—total noise signature measured by sensor FF021; red symbols—combustor-noise component using reference sensor NE801; blue symbols—combustor-noise component using reference sensor NE802; and gray symbols—coherence floor; engine power: (a) 50%, (b) 60%, (c) 70%, (d) 80%

Narrowband *SPL* results, for both the total-noise signature and its core/combustor-noise component, are shown in Boyle et al. [4, Figs. 10–13] for several engine-power settings at the 130° midfield and farfield locations. Here, Figs. 2 and 3 show the corresponding 1/3-octave *SPL* for the midfield and farfield locations used in Ref. 4, respectively, for the 1/3-octave frequency range of 100–2000 Hz. The total-noise-signature constant-percentage-binwidth (*CPB*) spectra are obtained simply by summing up the corresponding narrowband results, i.e, the total-noise results contain broadband as well as tonal contributions. Tones and harmonics associated with the shaft-passing frequencies of the low- and high-pressure spools (SPF_L and SPF_H), as well as some other discrete tones, are clearly visible in the narrowband combustor-noise[c] results presented in Boyle et al. [4], as well as in Hultgren [2]. Consequently, discrete tones need to be excluded during the summing up of the narrowband coherent-power spectrum in order to provide accurate *CPB* results for the broadband combustor-noise component. This is accomplished using a three-step process. In the first pass, the coherence between the two core-nozzle-exit sensors, NE801 and NE802, is used to identify the tones (eg. [4, Fig. 9]). The coherence between the far- or mid-field sensor of interest and the reference sensor at each so-identified tone is then replaced with an average of the two nearest non-tonal values, thus removing the tone from (or at a minimum reducing its impact on) the narrowband coherent-power spectrum. Even though this procedure is judged to be quite robust, it does not always eliminate all tones for the required frequency range of up to 2.239 kHz. A second pass is therefore

[c]Strictly speaking core-noise, since tones are not excluded

implemented. Its procedure identifies tones in the total-noise signature and adjusts the coherence values at those frequencies in a manner analogous to the previous pass. Even though this improves the situation, some tone remnants as well as additional unidentified tones are sometimes still observable in the coherent spectra after this second step. For simplicity, a third manual tone-removal step is therefore added to the overall process. This three-pass approach produces sufficiently 'clean' narrowband coherent-power spectra that are summed up to yield the corresponding *CPB* spectra. It is quite conceivable that the third step could be minimized, or maybe even eliminated, by adjustments to the threshold values used in the first two steps. However, this is not pursued further here. Miles' deliberately-detuned-coherence method [20, 21] or Sree's tone-broadband-separation method [22, 23] are alternative approaches that may be explored in future work.

Figure 2 shows the midfield results (MF101) for the 1/3-octave frequency range of 100 to 2000 Hz for four power settings, namely 50%, 60%, 70%, and 80%. The black, red, blue, and gray symbols denote the total signature, the combustor-noise component educed using the NE801 sensor or the NE802 sensor as reference signal, and the threshold value for the source-separation method. Any combustor-noise results below the latter would not be meaningful using the present source separation and data processing techniques. The presence of broadband combustor noise is evident in all of the panels, (a)–(d). Figure 3 shows the farfield results (FF021) for the 1/3-octave frequency range of 100 to 2000 Hz also for the four power settings of 50%, 60%, 70%, and 80%, using the same color key as above for the results. The presence of broadband combustor noise is also evident in the figure. As expected from the narrowband results presented in Boyle et al. [4], the *CPB* results obtained here also exhibit a second spectral hump when the 7 o'clock ITP (NE802) is the reference signal.

C. Combustor-Noise *OASPL*

Hultgren [2] suggested a thrust-class correction to the ANOPP GECOR predictions for the DGEN 380 turbofan. Good agreement with the 2014 test data was obtained by adjusting the total acoustic power level by -11.5 dB in the small-engine (SmE) method in combination with the PW turbine attenuation formula [2]. The proposed thrust-class correction was based on the thrust ratio of the two engine classes, very-light-jet engines (VLJ) and small engines (SmE). Using a thrust-class correction is not without precedent since this is really the difference between the original SAE method (1970s) and the newer small-engine method (1990s) in the GECOR module of ANOPP.

In order to further test this hypothesis, a more global validation was desired that also could potentially yield a better numerical estimate for the thrust-class correction. It is proposed to base this test on the combustor-noise component *OASPL* revealed by using the coherent-power source separation method employed herein. Based on the observed frequency range in Ref. 4 and here, the educed narrowband combustor-noise *SPL* is summed up from 112.2 Hz to 1,122.0 Hz (i.e., 1/3-octave bands higher than 100 Hz and up to and including 1,000 Hz contribute) to provide an estimated value for the *OASPL* at each available polar angle and engine-power setting (test point). The ANOPP GECOR directivity function, see Fig. 4, has a distinct peak at 120° which is well bracketed by the polar angles (approximately 108° through 143°) in the 2017 baseline core/combustor-noise test analyzed here (see Table 1).

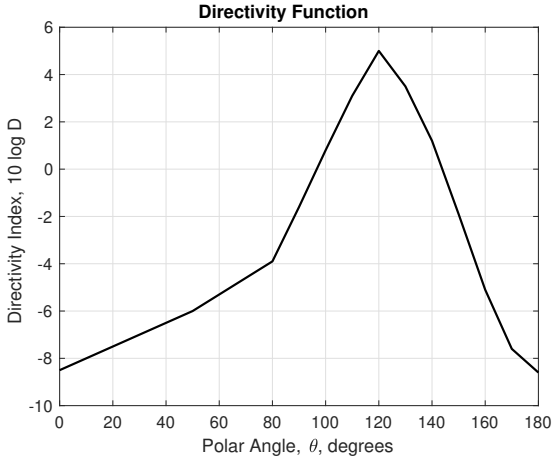


Fig. 4 ANOPP-GECOR directivity function, $D(\theta)$

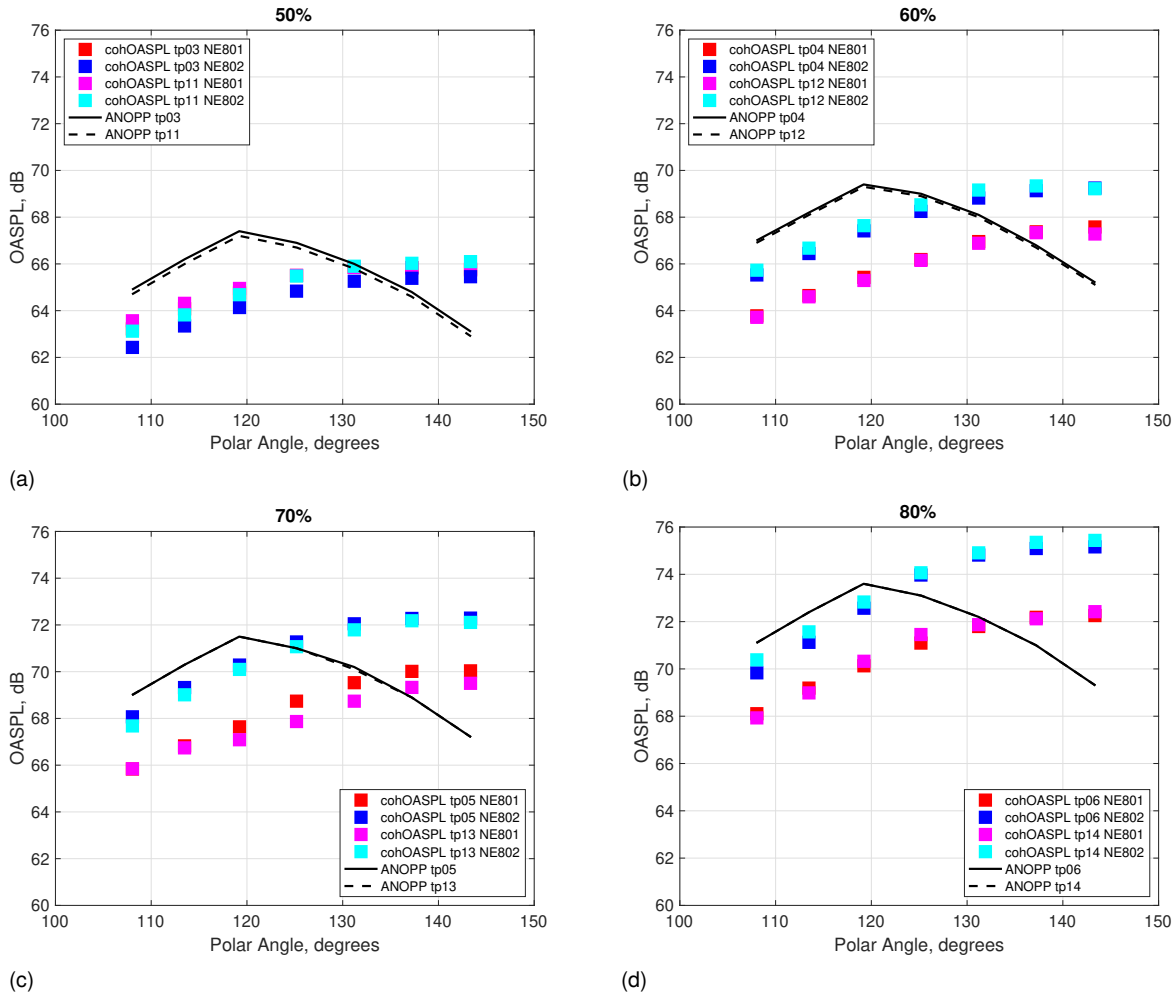


Fig. 5 Combustor-noise farfield *OASPL* versus polar angle; solid and dashed black lines—thrust-class corrected ANOPP prediction [2] for two equivalent-power test points, respectively; red and magenta symbols—reference sensor NE801; blue and cyan symbols—reference sensor NE802; red/blue and magenta/cyan symbol pairs represent different test points; engine power: (a) 50%, (b) 60%, (c) 70%, (d) 80%

The solid and dashed black lines in Fig. 5 represent ANOPP-GECOR *OASPL* predictions for the combustor noise using the small-engine (SmE) method with the PW turbine attenuation formula (SmE-PW configuration), including the effects of spherical spreading and atmospheric attenuation, for the actual conditions of each test point. See Section III above for more information about the combustor-noise models in ANOPP. The 'tp' notation in the legend indicates the test point, see Table 2. Note that the microphone locations are not at a fixed distance from the core-nozzle exit plane. Consequently, the virtual source predictions were propagated separately (using the actual distance) to each microphone location in the ANOPP-GECOR simulation.[d] A total-acoustic-power adjustment of -11.5 dB, as suggested by Hultgren [2], has been applied to the predictions before plotting. The symbols denote the experimental results processed as described in the previous subsection. The red and magenta colors indicate that the reference sensor NE801 was used to obtain the coherent-power results and the blue and cyan colors indicate usage of reference sensor NE802. The red/blue and magenta/cyan color pairs indicate that the results are from different test points at the same power setting. The figure shows results for the four engine-power settings of 50%, 60%, 70%, and 80% in panels (a) through (d).

In general, the present results indicate that a simple thrust-class acoustic-power correction alone is not sufficient to predict the combustor-noise *OASPL* educed from the measurements. On average, the applied correction leads to a reasonable prediction in the 130° direction when the sensor (NE801) located at the 6 o'clock nozzle-exit position

[d]With the slight differences in atmospheric attenuation ignored, the predictions for sensors FF017 and FF023 are, consequently about 0.3 dB less and 0.4 dB larger, respectively, than if they had been at the same distance as sensor FF019, which coincides with the theoretical peak direction.

provides the reference signal, which corresponds to the arrangement in Hultgren [2]. The results computed from the measurements seem to indicate that the combustor-noise *OASPL* peak value occurs for a polar angle of about 140° rather than the theoretical 120° value. However, measurements at larger polar angles would certainly be required to firm up this tentative observation. Nevertheless, it is clear that a directivity correction is needed in combination with an overall acoustic power correction to properly model the observations.

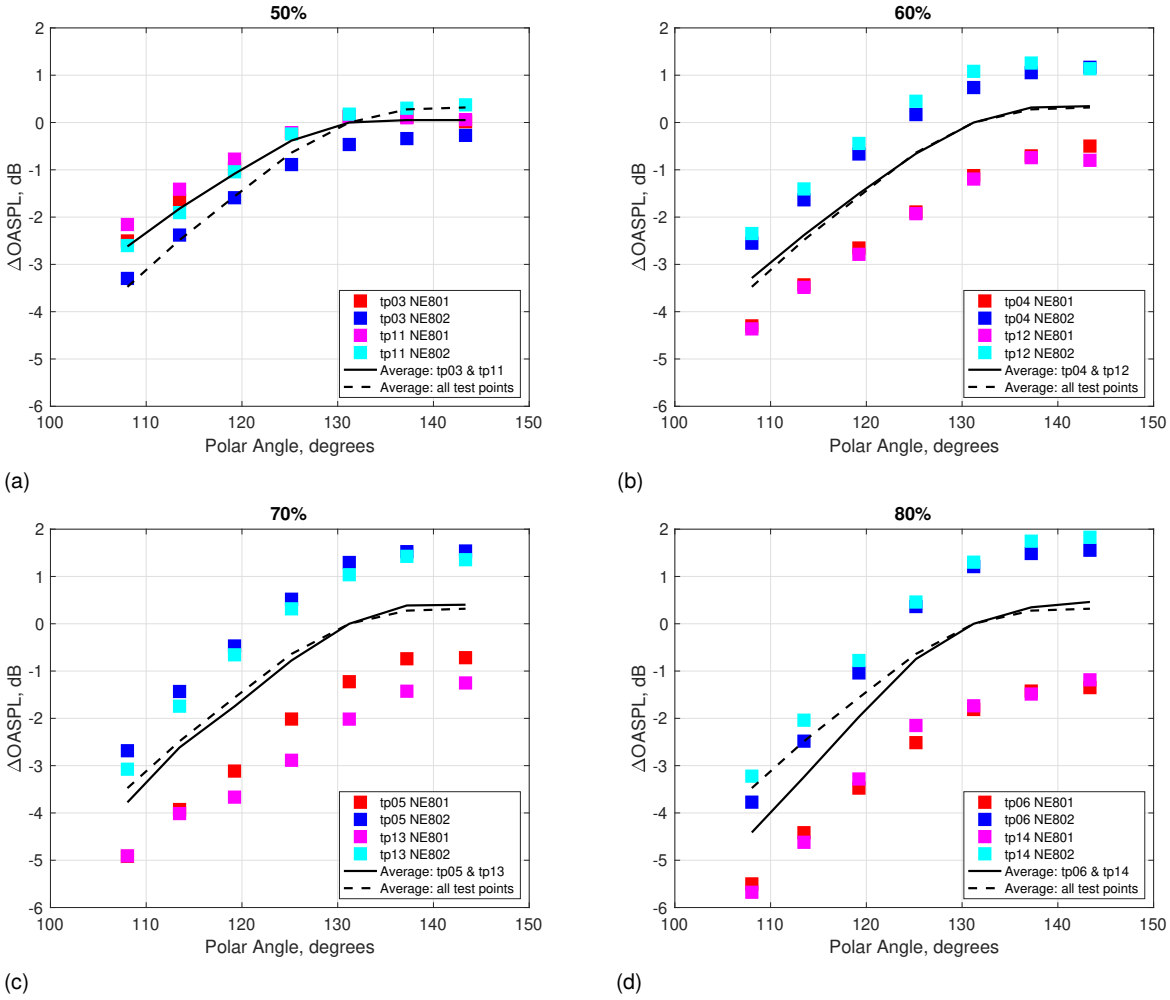


Fig. 6 Polar-angle dependency of combustor-noise farfield *OASPL*, normalized by average sensor-FF021 value for each engine power: (a) 50%, (b) 60%, (c) 70%, (d) 80%; solid and dashed black lines—average value at each engine-power setting and average over all four settings, respectively; red and magenta symbols—reference sensor NE801; blue and cyan symbols—reference sensor NE802; red/blue and magenta/cyan symbol pairs represent different test points

To further investigate the need for a directivity correction, the combustor-noise *OASPL* computed from the experimental data is normalized by the average of the sensor-FF021 values obtained for each engine-power setting. That is, the normalization is determined from two test points, each with values resulting from using the two different reference sensors. The normalized value $\Delta OASPL = OASPL - 10\log_{10}\left(\frac{1}{4}\sum_{k=1}^{4} 10^{L_k/10}\right)$, where L_k, k = 1–4, are the four combustor-noise *OASPL* values detected for the FF021 location. The farfield sensor FF021 was chosen here simply because it corresponds to the direction discussed in Hultgren [2]. Figure 6 shows the combustor-noise $\Delta OASPL$ for the engine-power settings of 50%, 60%, 70%, and 80%. The symbol color key is the same as in Fig. 5. The solid black lines represent the average value at each polar angle for the power setting in the subfigure. The dashed black lines represent the polar dependency of the average over all the power settings in this figure. First, the results obtained for each reference sensor appear quite repeatable, with the exception of the 50% power setting for reference sensor NE802

and the 70% power setting for reference sensor NE801. The deviation is less than 1 dB in both these cases however. Second, the overall-average curve tracks the engine-power-average curves well for the 60% and 70% power settings. The deviation is less than 1 dB for the other two settings. Third, the different reference-sensor results shown in Fig. 6(b)–(c) track each other and the average well in general, but are symmetrically offset from the power-level-average curve in each panel. The last observation indicates that a single directivity-correction function might not be a suitable approach. This conclusion can also be inferred directly from Fig. 5.

The clear difference between the combustor-noise *OASPL* levels detected using either the NE801 or NE802 sensors, Fig. 6(b)–(c), is due to the presence of the second hump in the *CPB* spectra, see Figs. 2 and 3, when NE802 is the reference sensor. As pointed out in Boyle et al. [4], the second hump in their coherent-power narrowband *SPL* spectra, when NE802 is the reference sensor (which here carries over into the *CPB* spectra), is quite possibly associated with the first azimuthal duct mode at the core-nozzle exit. It is therefore deemed necessary to document the unsteady pressure field at the core-nozzle exit in more detail before proceeding further with any modeling activities. An unsteady pressure survey using a circumferential ITP array at the core-nozzle exit is planned as part of a DART test in the NASA GRC AAPL facility scheduled for the second half of calender year 2019. Farfield microphone data will also be acquired simultaneously with the ITP-array data. The aim of this future effort is not only to document the modal structure (relevant to combustor noise) at the core-nozzle exit, but also to provide time-series data allowing the application of advanced source-separation methods [24] that combine correlation methods with mode-decomposition techniques.

V. Summary

A continued analysis of acoustic time-series data acquired during a baseline test [4] using the new DART resource at NASA Glenn Research Center is presented here, with particular emphasis on 1/3-octave analysis. The ultimate objective is to improve the prediction capability of the ANOPP module GECOR, which provides estimates of the combustor-noise component of airport-community noise. A first step in this endeavor is described in this paper.

The core-noise component of the total-noise signature at a given farfield-microphone location is obtained by applying a two-signal coherence method [5], commonly referred to as the coherent-power method, to the time-history data. Tones and harmonics associated with the shaft-passing frequencies of the low- and high-pressure spools, as well as some other discrete tones, are next excluded from the narrowband core-noise *SPL* spectra produced by the coherent-power method. The resulting combustor-noise *SPL* spectra are then summed up to yield the corresponding 1/3-octave *SPL* spectra for the combustor-noise component at a given farfield location. It is found that sufficient care must be taken to remove all tonal components in the relevant frequency range for combustor noise. Furthermore, as expected from the narrowband results presented in Boyle et al. [4], the 1/3-octave results also exhibit a second spectral hump when the 7 o'clock sensor at the core-nozzle exit provides the reference signal. This second hump is possibly associated with the presence of a first azimuthal duct mode at the core-nozzle exit.

Next, 1/3-octave *SPL* spectra are summed up over a relevant 1/3-octave center-frequency range to provide estimates of the combustor-noise *OASPL*. The results indicate some degree of merit for the proposed concept of a thrust-class correction for this class of engines [2]. However, it is clear that directivity correction is also needed. Furthermore, the results indicate that the combination of a single acoustic-power correction and a universal directivity correction applied to the present ANOPP GECOR prediction model would not sufficiently well capture the *OASPL* computed from the experimental data. This difficulty is believed to caused by the possible propagation of the first azimuthal mode inside the combustor to the exterior for this particular turbofan engine. The results reported on here without doubt indicate the need for measurements to document the modal-structure of the unsteady pressures at at the DART core-nozzle exit. A better understanding of the core-nozzle-exit modal structure, relevant to combustor noise, is essential for further progress.

Appendices

A. Mean-Line Data

The DGEN 380 turbofan FADEC provides select performance data at a rate of 1 sample per second. Table A 1 shows relevant sensor details pertaining to the core. The notational convention adopted here is that the subscript indicating the turbomachinery station is prefixed by a 't' for total properties, whereas no prefix is used for static variables. DGEN-external ambient temperature and relative humidity measurements, T_{ext} and H_{ext}, are also reported by the FADEC. In addition, the FADEC provides computed values of the combustor mass-flow rate, w_{32}, and the total temperature after the turbine-inlet guide vanes, T_{t41}, at each sample point. The FADEC provided data were averaged over the duration of each test point to yield pertinent mean-flow values.

Table A 1 DGEN 380 Core Performance Data

Type	Variable	Number of Sensors	Number of Ports	Location
Ambient pressure	P_{amb}	1	-	Control bay
Ambient temperature	T_{amb}	1	-	Control bay
Low-spool speed	N_L	2	-	Engine
High-spool speed	N_H	2	-	Engine
Static pressure	P_3	1	3	Station 3
Total temperature	T_{t3}	3	-	Station 3
Fuel volumetric flow rate	$\dot{q}_F$	1	-	Fuel supply
Fuel pressure	P_F	1	-	Engine
Fuel temperature	T_F	3	-	Fuel supply
Total pressure	P_{t5}	4	12	Station 5
Total temperature	T_{t5}	12	-	Station 5
External temperature	T_{ext}	1	-	DART external
Relative humidity	H_{ext}	1	-	DART external

1. Ambient Conditions

Table A 2 lists the ambient conditions determined from the FADEC output for the different test points, their average values, as well as the sea-level standard conditions. The specific humidity, expressed as a mole fraction, $\mathcal{H}_{\text{mole}}$ is computed from H_{ext} using (B 10). As can be seen, the specific humidity did not vary significantly during the test campaign. As a simplification, the average value, 2.029%, can therefore be used to construct a single tabulation of the thermodynamic properties (see Appendix B) needed for the mean-line computations upstream of the combustor rather than having to construct one such table for each test point.

2. Turbofan Station 3

Station 3 is located after the diffuser of the high-pressure compressor and, thus, describes the inlet conditions for the combustor. Three static pressure ports, all fed to a single transducer, and three total temperature sensors, provide input for the determination of the mean-line conditions P_3 and T_{t3}. The static temperature, T_3, is then determined from

$$V_3 = \dot{m}_3 R T_3 / P_3 A_3, \tag{A 1a}$$

$$h_s(T_{\text{t3}}) = h_s(T_3) + \tfrac{1}{2} V_3^2, \tag{A 1b}$$

where A_3 is the cross-sectional area, $\dot{m}_3 = w_{32}$ is the mass-flow rate, and V_3 is the mean-line velocity (all) at station 3. The iterative procedure utilized here for solving this set of equations is to take T_{t3} as an initial guess for T_3 in (A 1a), next solve (A 1b) for T_3 using (reverse) interpolation in the appropriate sensible enthalpy table, and then repeat this process until sufficient convergence is obtained. The total pressure P_{t3} is then obtained using (B 9). The engine overall pressure ratio,

$$OPR = P_{\text{t3}} / P_{\text{amb}}, \tag{A 2}$$

can thus be determined for each test point. Note that for the test points investigated here, the relative difference between total and static variables for the pressure and temperature are within 0.7% and 0.2%, respectively. Consequently, the common approximation that total and static variables are equal at the compressor diffuser exit holds true here.

Table A 2 Ambient Conditions

Point #	P_{amb}, kPa	T_{amb}, K	H_{ext}, %	$\mathcal{H}_{mole}$, %
1	98.4	298.66	60.52	2.009
2	98.4	298.69	59.85	1.991
3	98.4	298.70	60.60	2.017
4	98.4	298.75	59.85	1.998
5	98.4	298.83	60.42	2.027
6	98.4	298.90	60.46	2.037
7	98.4	298.90	60.59	2.041
8	98.4	298.84	61.14	2.052
9	98.4	298.89	60.98	2.053
10	98.4	298.91	60.70	2.045
11	98.4	298.92	60.24	2.031
12	98.4	298.92	60.41	2.037
13	98.4	299.00	60.25	2.041
14	98.4	298.97	60.48	2.045
15	98.4	299.00	60.35	2.045
16	98.4	299.13	58.38	1.993
Average	98.4	298.88	60.33	2.029
SLS	101.325	288.15	70.00	1.178

3. Turbofan Station 4

Station 4 is located at the combustor exit, i.e. somewhere ahead of the turbine-inlet guide vanes. The combustion process is assumed to take place at constant pressure. Hence,

$$P_4 = P_3\,, \tag{A 3}$$

under idealized conditions. Conservation of mass requires that

$$\dot{m}_4 = \dot{m}_3 + \dot{m}_F = (1 + f)\dot{m}_3\,, \tag{A 4}$$

where $\dot{m}_F$ is fuel mass-flow rate and $f = \dot{m}_F/\dot{m}_3$ is the fuel-to-air mass ratio. Under the assumption that there is no heat transfer to the surroundings during the combustion process, the conservation of energy is, to sufficient accuracy, described by

$$(1 + f)h_s(T_{t4},\ f) = h_s(T_{t3}) + f h_{PR}\,, \tag{A 5}$$

where h_{PR} is the constant-pressure heating value of combustion. It is the difference in the enthalpy of formation of the reactants and products, respectively, when complete combustion occurs at a given pressure. It represents the amount of heat that would have to be removed to keep the temperature constant. Note that the sensible enthalpy at the combustor exit also depends on the fuel-to-air mass ratio since the reaction changes the mixture composition.

a. Fuel Properties

A description and history of aircraft fuels can be found in the CRC Handbook of Aviation Fuel Properties [25], which points out that aviation fuels are generally specified based on usage requirements rather than their detailed chemistry. Aviation turbine, or jet, fuels, are essentially straight-run distillates and their primary characteristics therefore depend on the crude-oil type. Their overall composition has changed relatively little over time, but they now have the most extensive specifications of all fuels. In general, aviation turbine fuels are required to be solely hydrocarbon compounds with select approved additives. Certain hydrocarbon types, eg. aromatics, are limited by fuel and engine-system performance requirements. For the fuels Jet A/A-1, the U. S. commercial-turbine-fuel specifications [25, Table 1-3] gives the range of 775–840 kg/m^3 for the density at 288.15K and the minimum requirement of 42.8 MJ/kg for the heating value of combustion. However, the CRC report [25, Fig. 2-1] illustrates the typical variation of density with temperature for major jet fuels. For Jet A-1, a fit of the data in this figure implies that

$$\rho_F = 804 - 0.7 \times (T_F - 288.15)\ \text{kg/m}^3\,, \tag{A 6}$$

where ρ_F and T_F are the density (kg/m^3) and temperature (K) of the fuel. The CRC report (Ref. 25, Table 2-2) also lists typical values for the net heat of combustion. For Jet A/A-1 this value is

$$h_{PR} = 43.2\,\mathrm{MJ/kg} \tag{A 7}$$

and this is the value used herein.

The test-point averaged FADEC-provided performance data, see Table A 1, includes the volumetric flow rate and temperature of the fuel. After converting the former from the conventional units of l/h (liter per hour) to the consistent SI units of m^3/s, the fuel-to-air ratio is obtained from

$$f = \rho_F \dot{q}_F / \dot{m}_3\,, \tag{A 8}$$

where ρ_F is determined by (A 6).

b. Mixture Properties Downstream of Combustor

In contrast to the situation upstream of the combustor, the thermodynamic properties, like the sensible enthalpy, also now depend on the fuel-to-air mass ratio since the combustion process changes the mixture composition. Jet fuel is made up of a very large number of hydrocarbon species mainly belonging to, in alphabetical order, the aromatic, naphthalene, olefin, and paraffin families. The detailed composition depends on the crude oil used in its production, i.e. not only on the manufacturer, but also from where the refinery was supplied.

The simplifying assumption is made here that all the hydocarbons in the fuel belong to the olefin family. While strictly speaking not true, there is precedent [26, Section 2.6.7] for this approximation. In this case, it is relatively straight forward to construct tables of the needed thermodynamic properties as functions of the temperature, specific humidity, and fuel-to-air ratio. In particular, the sensible specific enthalpy is given by (C 16), where (C 16b) can be replaced by

$$\Delta h_s(T) \equiv [(1 + f_S)h_s(T, f_S) - h_s(T, 0)]/f_S\,, \tag{A 9}$$

with f_S being the stoichiometric fuel-to-air ratio. Analogous formulas apply for the specific heat at constant pressure $c_p(T, f)$, the specific entropy function $s^{(o)}(T, f)$, as well as the gas constant $R(f)$, see Appendix C for more details. Since the specific humidity is taken as a constant during this test campaign, it follows that only two tables need to be precomputed for each thermodynamic property in order to determine a value at a given temperature and fuel-to-air ratio.

c. Conditions Downstream of Combustor

Equation (A 5) can now be solved for $T_{\mathrm{t}4}$ through reverse interpolation in the look-up table for the sensible specific enthalpy. Figure 7(a) compares $T_{\mathrm{t}4}$ (red symbols), computed with a relative humidity of 60.33% assumed for the ingested air, to the FADEC-provided $T_{\mathrm{t}41}$ (blue symbols). The DGEN 380 turbofan does not have any cooling of the turbine-inlet guide vanes (neither film nor internal cooling flows) so ideally these two total temperatures should be equal. Note that at present, the authors do not have any information about how the FADEC actually computes $T_{\mathrm{t}41}$ from the engine-performance measurements, see Table A 1. As a comparison, Figure 7(b) shows the corresponding results with $T_{\mathrm{t}41}$ (magenta symbols) determined assuming dry air as the working gas. With the exception of the idle test points (1, 2, 9, and 10 at 33% power), the two computations essentially bracket the FADEC-provided $T_{\mathrm{t}41}$, with the humid and dry air cases being lower and higher, respectively. These two subfigures also show the FADEC-provided measurement of the turbine-exit total temperature $T_{\mathrm{t}5}$ (cyan symbols). As can be expected, the total temperature drop is quite small across the turbine at engine-idle test points. For test point 9, the humid-air results for $T_{\mathrm{t}4}$ is actually about 2 K lower than the $T_{\mathrm{t}5}$ measurement, which is clearly an unphysical result. However, this amount likely is smaller than the uncertainty in the mean-line computations which is expected to be of the order of a couple of percent at best. The analysis will proceed using the humid-air results as a basis herein, with some caution applied if interpreting engine-idle results.

The acoustic impedance at turbofan station 4 is given by

$$Z_4 = \rho_4 c_4 = P_4 \sqrt{\frac{\gamma(T_4)}{RT_4}}\,, \tag{A 10}$$

where ρ_4 and $c_4 = \sqrt{\gamma(T_4)RT_4}$ are the local density and speed of sound, respectively. Because of the high temperature at the combustor exit, the corresponding Mach number will be quite small (typically of the order of 0.1) and the static temperature is then approximately equal to the total temperature, i.e. $T_4 \approx T_{\mathrm{t}4}$. Using this approximation in (A 10) then leads to a reasonable estimate for the acoustic impedance at station 4.

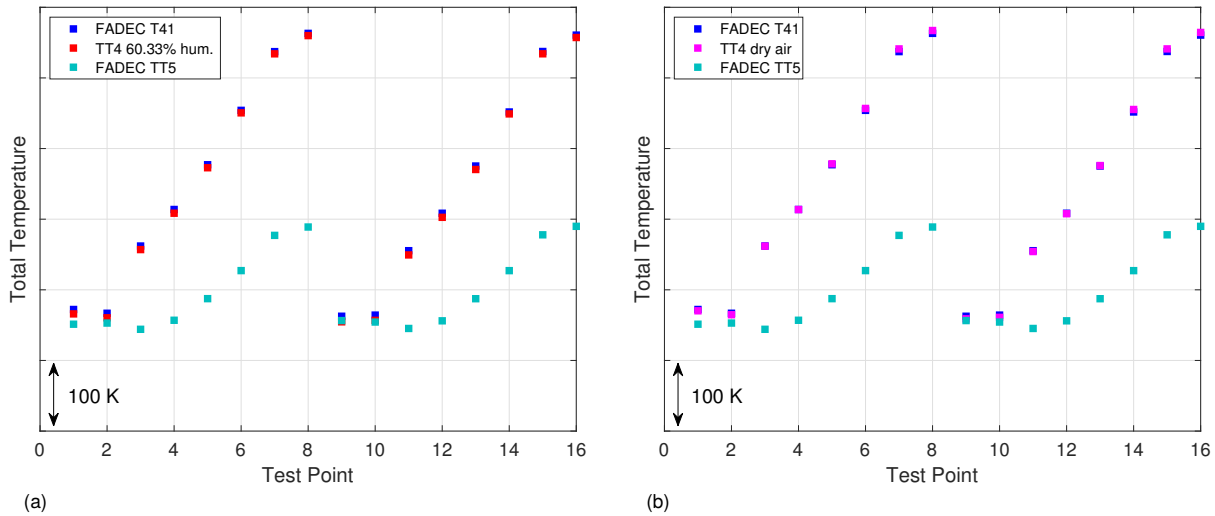


Fig. 7 Total temperatures at turbofan stations 4 (red and magenta), 41 (blue) and 5 (cyan); T_{t4} determined using (a) 60.33% relative humidity air and (b) dry air; T_{t41} provided by FADEC computation; T_{t5} FADEC-provided measurement.

4. Turbofan Station 5

Station 5 is located just downstream of the low-pressure-turbine exit and describes the outlet conditions of the turbine. There are three radial total-pressure rakes at this station. They are equidistantly spaced in the circumferential direction and each have four pressure ports (i.e. 12 ports in total). The pressure ports are fed to four transducers with each transducer receiving input from the three ports at the same radial distance in the duct. Clocked in between these rakes are three rakes each instrumented with four total temperature thermocouples. The average of these two sets of sensors determines the mean-line conditions P_{t5} and T_{t5}. The static pressure and temperature, P_5 and T_5, are then determined from

$$V_5 = \dot{m}_5 R T_5 / P_5 A_5, \tag{A 11a}$$

$$h_s(T_{t5}) = h_s(T_5) + \tfrac{1}{2} V_5^2, \tag{A 11b}$$

and (B 9), where A_5 is the cross-sectional area, $\dot{m}_5 = (1 + f)\, w_{32}$ is the mass-flow rate, and V_5 is the mean-line velocity (all) at station 5. The iterative procedure used here for solving this set of equations is to take P_{t5} and T_{t5} as initial guesses for P_5 and T_5 in (A 11a), next solve (A 11b) for T_5 using (reverse) interpolation in the appropriate sensible enthalpy table, finally get an updated value for P_5 using (B 9), and then repeat this process until sufficient convergence is obtained.

The acoustic impedance at turbofan station 5 is given by

$$Z_5 = \rho_5 c_5 = P_5 \sqrt{\frac{\gamma(T_5)}{R T_5}}, \tag{A 12}$$

where ρ_5 and $c_5 = \sqrt{\gamma(T_5) R T_5}$ are the local static density and speed of sound, respectively.

B. Basic Thermodynamic Relationships

A non-reacting ideal gas is described by the gas law

$$P = \rho R T, \tag{B 1}$$

where P, ρ, and T are the pressure, density, and temperature (all are static or state variables) and R denotes the gas constant; and the equation of state

$$h = h_f^o + \int_{T_f}^{T} c_p(T')\mathrm{d}T', \tag{B 2}$$

where h is the specific enthalpy, $c_p(T)$ is the specific heat at constant pressure, h_f^o is the enthalpy of formation (25^o C = 298.15 K, 100 kPa), and $T_f = 25^o$C = 298.15K. The integral on the right-hand side is often referred to as the sensible enthalpy. The specific enthalpy and internal energy e are related through

$$h = e + \frac{P}{\rho}, \tag{B 3}$$

and, hence, the internal energy of the gas is given by

$$e = \int_{T_f}^{T} c_v(T')\mathrm{d}T' - RT_f + h_f^o\,, \tag{B 4}$$

where $c_v(T)$ is the specific heat at constant volume. The first two terms are referred to as the sensible internal energy and the last term, the enthalpy of formation, is referred to as the chemical energy. Note that the sensible internal energy is not zero at the formation reference state. The specific entropy s is given by

$$s(T,P) = s^{(o)}(T) - R\ln(P/P_f)\,, \tag{B 5a}$$

where $P_f = 100\,$kPa, i.e. the reference state is taken as the state at formation, and

$$s^{(o)}(T) = s_f^{(o)} + \int_{T_f}^{T} \frac{c_p(T')}{T'}\mathrm{d}T'\,. \tag{B 5b}$$

The total specific enthalpy is defined as

$$h_t = h + \tfrac{1}{2}u_i^2 = h(T) + \tfrac{1}{2}\gamma(T)RTM^2\,, \tag{B 6}$$

where u_i is a velocity component, u_i^2 denotes the square of the velocity-vector magnitude, $\gamma = c_p/c_v$ is the ratio of specific heats at constant pressure and volume, respectively, and

$$M = \sqrt{u_i^2/\gamma(T)RT} \tag{B 7}$$

is the Mach number, with $c = \sqrt{\gamma(T)RT}$ being the local speed of sound.

The total temperature T_t can now be introduced as follows

$$h(T_t) = h(T) + \tfrac{1}{2}\gamma(T)RTM^2\,. \tag{B 8}$$

T_t is the temperature that when inserted into (B 2) yields the same value as (B 6) evaluated for the corresponding static temperature T and Mach number M. The isentropic stagnation state is the state that the flowing gas would attain if it underwent a reversible adiabatic deceleration to rest. Thus, the total temperature $T_t = T_t(T,M)$ is simply the isentropic stagnation temperature. Analogously, the total pressure is just the isentropic stagnation pressure and it follows from (B 5a) that

$$P_t = P\exp\left\{\frac{1}{R}\left[s^{(o)}(T_t) - s^{(o)}(T)\right]\right\}\,. \tag{B 9}$$

For a perfect gas, the specific heats c_p and c_v, and consequently also γ, are constant and the enthalpy of formation $h_f^0 = c_pT_f$. In this case, much simpler formulas corresponding to (B 2), (B 4)–(B 9), as usually seen in elementary treaties of gas dynamics, can be written down. Because of the large temperature changes experienced by the mean-line flow in turbomachinery, this further simplified approach will not be followed here, however.

Instead, tables are constructed containing the specific heat at constant pressure c_p, the ratio of specific heats γ, the sensible enthalpy $h_s \equiv h - h_f^o$, and the entropy function $s^{(o)}$ as functions of the static temperature T for given humidity levels. Required properties can then be obtained by interpolation in these tables. The molecular weights of dry-air, its components, water vapor, and, as an example, olefin hydrocarbon fuels (i.e. C_nH_{2n}, with $n \geq 2$), are given in the Table B 1.

Humidity is commonly expressed as relative humidity $\mathcal{H}_{\mathrm{rel}}$ in percent, i.e. this is usually the output of meteorological instrumentation. However, from a physical, or computational, point of view the more relevant variable is the specific

Table B 1 Molecular weights

component	molecular weight	dry-air mole fraction, %	dry-air mass fraction, %
N_2	28.013	78.09	75.526
O_2	31.999	20.95	23.145
Ar	39.948	0.93	1.283
CO_2	44.010	0.03	0.046
dry-air	28.964	100	100
H_2O	18.015	-	-
C_nH_{2n}	$14.027n$	-	-

humidity, $\mathcal{H}_{\text{mole}}$, i.e. the mole ratio of water vapor molecules to the total number of molecules in the gas. The ANOPP documentation gives the following conversion formula:

$$\mathcal{H}_{\text{mole}} = \mathcal{H}_{\text{rel}}(P_{\text{SLS}}/P) \times 10^{8.4256 - 10.1995(T_{\text{SLS}}/T) - 4.992\log(T/T_{\text{SLS}})} . \tag{B 10}$$

The textbook by Van Wylen and Sonntag (Ref. 27, Table A.9) contains empirical fits for $\bar{c}_p(T)$, where the 'overbar' indicates that the quantity is on a per-mol rather than unit-weight basis, for nitrogen N_2, oxygen O_2, carbon dioxide CO_2, and water vapor H_2O among other ideal gases. These expressions can be integrated, see (B 2) and (B 5), to yield expressions for $\bar{h}_s(T)$ and $\bar{s}^{(o)}(T)$, where the constants of integration are determined by $\bar{h}_s(T_f) = 0$ and values for $\bar{s}^{(o)}(T_f)$ that can be found in Van Wylen and Sonntag (Ref. 27, Table A.11). Corresponding results for argon Ar are directly available from a web publication/database [28] of the U.S. National Institute of Standards and Technology (NIST). Given the mole fraction of the constituents of moist air, the required tabulation is then performed. The specific heat at constant pressure and the sensible enthalpy of the multi-species ideal gas are then given by

$$c_p(T) = \sum_{k=1}^{N} Y_k c_{p,k} = \frac{1}{W}\sum_{k=1}^{N} X_k \bar{c}_{p,k} , \tag{B 11a}$$

$$h_s(T) = \sum_{k=1}^{N} Y_k h_{s,k} = \sum_{k=1}^{N} Y_k \int_{T_f}^{T} c_{p,k}(T')\mathrm{d}T' = \frac{1}{W}\sum_{k=1}^{N} X_k \int_{T_f}^{T} \bar{c}_{p,k}(T')\mathrm{d}T' = \frac{1}{W}\sum_{k=1}^{N} X_k \bar{h}_{s,k} , \tag{B 11b}$$

where Y_k denotes the mass fraction of component k in the mixture, $X_k = Y_k W/W_k$ is the corresponding mole fraction, W_k is the molecular weight of species k, and $W = 1/\sum_{k=1}^{N}(Y_k/W_k) = \sum_{k=1}^{N} X_k W_k$ is the total molecular weight of the mixture. Analogous formulas apply for the enthalpy of formation and the entropy function $s^{(o)}$.

The gas constant of the mixture is given by

$$R = \bar{R}/W , \tag{B 12a}$$

where $\bar{R} = 8.31434\,\text{J/mol K}$ (Ref. 27, p. 44) is the universal gas constant. Finally, the ratio of specific heats of the mixture is given by

$$\gamma(T) = c_p/(c_p - R) = \bar{c}_p/(\bar{c}_p - \bar{R}) . \tag{B 12b}$$

C. Multi-Species Reacting Gas

Most air-breathing gas-turbine engines use hydrocarbon fuels. Assuming that all fuel components belong to the olefin family, i.e. C_nH_{2n}, with $n \geq 2$, even though not quite true in practice, greatly simplifies the chemical reaction balance while yet producing representative numerical results. For air-breathing, olefin-fueled combustors, the basic combustion process can be reduced to the following reaction:

$$C_nH_{2n} + \tfrac{3n}{2}O_2 \rightarrow nCO_2 + nH_2O . \tag{C 1}$$

For each mole of olefin fuel, $\frac{3n}{2}$ moles of oxygen is used and n moles of carbon-dioxide and water vapor is produced. This information can be used to construct tables for the relevant thermodynamic properties of the ideal-gas mixture resulting from the olefin-fuel combustion process as functions of the temperature and fuel-to-air mass ratio. The molecular weights of olefin hydrocarbon fuels, dry-air components, and water vapor are given in Table B 1.

1. Chemical Reaction

The general reaction, with oxygen as the oxidizer, corresponding to (C 1) can be written as

$$\nu'_F(Fuel) + \nu'_{O_2}(Oxidizer) + (Additional\ Components) \rightarrow (Products) + (Additional\ Components), \tag{C 2}$$

where ν' denotes the number of moles, the subscripts 'F' and 'O_2' denote fuel and oxidizer, respectively, and *'(Additional Components)'* indicates species in the mixture that do not take part in the chemical reaction. The mass stoichiometric ratio is defined as

$$S = (\nu'_{O_2} W_{O_2} / \nu'_F W_F), \tag{C 3}$$

where W_{O_2} and W_F are the molecular weights of the oxidizer and the fuel, respectively. It follows from (C 1) and Table B 1 that $S = 3.422\ldots$ for an Olefin based fuel.

It is customary to introduce the equivalence ratio ϕ for a given mixture as

$$\phi = \frac{S Y_F}{Y_{O_2}}, \tag{C 4}$$

where Y_{O_2} and Y_F denote the mass fractions of the oxidizer and the fuel. If $\phi < 1$, then the oxidizer is in excess and the combustion (if it occurs) is labeled lean; and if $\phi > 1$, then the fuel is in excess and the combustion is referred to as rich. Since the mass fractions have to sum up to unity, it follows that

$$Y_F + Y_{O_2} + Y_A = 1, \tag{C 5}$$

where Y_A denotes the mass fraction of the additional components, i.e. the water vapor due to humidity and the components of dry air in addition to oxygen in the cases of interest here. Equations (C 4) and (C 5 imply that

$$Y_F = \left[1 + \frac{S}{\phi}\left(1 + \frac{Y_A}{Y_{O_2}}\right)\right]^{-1}. \tag{C 6}$$

Since

$$1 + \frac{Y_A}{Y_{O_2}} = 1 + \frac{m_{H_2O} + m_{air} - m_{O_2}}{m_{O_2}} = \frac{m_{air}}{m_{O_2}}(1 + \mathcal{X}) = 4.321(1 + \mathcal{X}), \tag{C 7}$$

where the subscript 'air' indicates dry air and $\mathcal{X} \equiv m_{H_2O}/m_{air} = 0.6220\mathcal{H}_{\rm mole}/(1 - \mathcal{H}_{\rm mole})$, it follows that

$$Y_F = \left[1 + 4.321\frac{S}{\phi}(1 + \mathcal{X})\right]^{-1} = \left[1 + \frac{14.786}{\phi}(1 + \mathcal{X})\right]^{-1}, \tag{C 8}$$

where the last step is for the olefin family of fuels. Consequently, the stoichiometric fuel mass ratio in dry air is typically about 0.063 for the olefin family of fuels, which is a rather small value. Thus, the combustion products will not significantly change the functional temperature dependence of gas properties such as the heat capacity, etc. Finally, the commonly used fuel-to-air ratio is given by

$$f \equiv \frac{Y_F}{1 - Y_F} = \frac{\phi}{14.786(1 + \mathcal{X})} \tag{C 9}$$

for olefin fuels. Hence, the stoichiometric fuel-to-air ratio in dry air is about 0.0676.

2. Chemical Kinetics

In general, the N species reacts through M reactions, which can be expressed as

$$\sum_{k=1}^{N} \nu'_{kj} \mathcal{M}_k \rightarrow \sum_{k=1}^{N} \nu''_{kj} \mathcal{M}_k \quad \text{for} \quad j = 1, 2, \ldots, M, \tag{C 10}$$

where $\mathcal{M}_k$ symbolizes species k and ν'_{kj} and ν''_{kj} denote the molar stoichiometric coefficients of species k in reaction j. The conservation of mass requires that

$$\sum_{k=1}^{N} \nu_{kj} W_k = 0 \quad \text{for} \quad j = 1, 2, \ldots, M, \tag{C 11}$$

where $\nu_{kj} = \nu''_{kj} - \nu'_{kj}$. The mass reaction rate for species k is the sum of the reaction rates produced by the M reactions, i.e.

$$\dot{\omega}_k = \sum_{j=1}^{M} \dot{\omega}_{kj} = W_k \sum_{j=1}^{M} \nu_{kj} Q_j \,, \tag{C 12}$$

where Q_j is the progress rate of reaction j. Note that, in view of (C 11),

$$\sum_{k=1}^{N} \dot{\omega}_k = \sum_{j=1}^{M} Q_j \left(\sum_{k=1}^{N} \nu_{kj} W_k \right) = 0 \tag{C 13}$$

and, hence, global mass is conserved.

Assuming only the one-step olefin-family reaction (C 1) is in play, it follows from (C 12) that the mass reaction rates for air can be expressed in terms of the fuel reaction rate as

$$\dot{\omega}_{N_2} = \dot{\omega}_{Ar} = 0 \,, \tag{C 14a}$$

$$\dot{\omega}_{O_2} = -S\dot{\omega}_F = -\frac{\frac{3}{2} W_{O_2}}{W_{CH_2}} \dot{\omega}_F = -3.422 \dot{\omega}_F \,, \tag{C 14b}$$

$$\dot{\omega}_{C_2O} = \frac{W_{CO_2}}{W_{CH_2}} \dot{\omega}_F = 3.138 \dot{\omega}_F \,, \tag{C 14c}$$

and

$$\dot{\omega}_{H_2O} = \frac{W_{H_2O}}{W_{CH_2}} \dot{\omega}_F = 1.284 \dot{\omega}_F \,, \tag{C 14d}$$

where $\dot{\omega}_F > 0$ implies that fuel is being consumed by the combustion process.

3. Mixture Properties After Combustion

Using a prime to indicate values after the complete chemical reaction, the mass fractions of the resulting mixture are given by

$$Y'_k = (Y_k + f C_k)/(1 + f) \,, \tag{C 15}$$

where Y_k are the mass fractions of the mixture before adding the fuel and C_k are the mass conversion factors for the reaction. For a one-step reaction of the olefin family of fuels, these conversion factors are simply given by the coefficients on the right-hand side of (C 14). Note that conservation of mass requires that $\sum_{k=1}^{N} C_k = 1$.

It follows that the sensible specific enthalpy after the reaction is given by

$$h_s(T, f) = [h_s(T) + f \Delta h_s(T)]/(1 + f) \,, \tag{C 16a}$$

where the prime has been dropped for simplicity of notation and

$$\Delta h_s(T) = \sum_{k=1}^{N} C_k h_{s,k}(T) \,. \tag{C 16b}$$

Identical formulas apply for the specific heat at constant pressure, $c_p(T, f)$ and the specific entropy function $s^{(o)}(T, f)$. Formulas like these have been given by Mattingly [26], p. 91. The gas constant after the completed reaction is given by

$$R(f) \equiv R' = \frac{\bar{R}}{W'} = \bar{R} \sum_{k=1}^{N} \frac{Y'_k}{W_k} = (R + f \Delta R)/(1 + f) \,, \tag{C 17a}$$

where

$$\Delta R = \bar{R} \sum_{k=1}^{N} \frac{C_k}{W_k} \,. \tag{C 17b}$$

This result implies that Eq. 2.64a in Mattingly [26] may be incorrect, or at best only an approximate result.

4. Heating Value

The heat release due to the one-step chemical reaction is given by

$$\dot{\omega}_T = -\sum_{k=1}^{N} \dot{\omega}_k h^0_{k,f} = -Q \sum_{k=1}^{N} \nu_k W_k h^0_{k,f} \,. \tag{C 18}$$

It follows that

$$\dot{\omega}_T = h_{PR} \dot{\omega}_F \,, \tag{C 19}$$

where

$$h_{PR} = \sum_{k=1}^{N} \nu_k W_k h^0_{k,f} / \nu_f W_F \tag{C 20}$$

is the constant-pressure heating value of the combustion and it represents the amount of heat that would have to be removed to keep the temperature constant during constant-pressure combustion. For the Olefin family of fuels (see Van Wylen and Sonntag [27], p. 506), the constant-pressure heating value, h_{PR}, ranges from 44.410 MJ/kg (Decene $C_{10}H_{20}$) to 47.158 MJ/kg (Ethene C_2H_4) at 25° C and 100 kPa. The heating value depends weakly on temperature, but this variation is commonly ignored. The minimum heating value for most civilian jet fuels is 42.8 MJ/kg (18400 Btu/lbm), see Table 1-3 in Ref. 25 or Mattingly [26], pp. 757-8. A typical (Ref. 25, Table 2-2) heating value is 43.2 MJ/kg (18570 Btu/lbm). The Camelia alternate fuel has a heating value of 43.3 MJ/kg.[e]

References

[1] Berton, J. J., "System Noise Prediction of the DGEN 380 Turbofan Engine," *J. Aircraft*, Vol. 53, No. 6, 2016, pp. 1779–1786. doi:10.2514/1.C033616.

[2] Hultgren, L. S., "A First Look at the DGEN380 Engine Acoustic Data From a Core-Noise Perspective," Tech. Rep. NASA/TM–2015-218924, NASA, 2015.

[3] Sutliff, D. L., Brown, C. A., Bayon, B., and Sree, D., "Farfield Acoustic Characteristics of the DGEN380 Turbofan Engine as Measured in the NASA Glenn Aero-Acoustic Propulsion Laboratory," AIAA Paper 2016-3006, 22nd AIAA/CEAS Aeroacoustic Conference, Lyon, France, 2016. doi:10.2514/6.2016-3006.

[4] Boyle, D. K., Henderson, B. S., and Hultgren, L. S., "Core/Combustor-Noise Baseline Measurements for the DGEN Aeropropulsion Research Turbofan," AIAA Paper 2018-3281, 24th AIAA/CEAS Aeroacoustics Conference, Atlanta, GA, 2018.

[5] Bendat, J. S., and Piersol, A. G., *Engineering Applications of Correlation and Spectral Analysis*, Wiley-Interscience, 1980.

[6] Zorumski, W. E., "Aircraft Noise Prediction Program Theoretical Manual, Part 1," Tech. Rep. NASA-TM-83199-PT-1, NASA, 1982.

[7] Zorumski, W. E., "Aircraft Noise Prediction Program Theoretical Manual, Part 2," Tech. Rep. NASA-TM-83199-PT-2, NASA, 1982.

[8] Ahuja, K. K., "Designing Clean Jet-Noise Facilities and Making Accurate Jet-Noise Measurements," *International J. Aeroacoustics*, Vol. 2, No. 3&4, 2003, pp. 371–412. doi:https://doi.org/10.1260/147547203322986188.

[9] Emmerling, J. J., Kazin, S. B., and Matta, R. K., "Core Engine Noise Control Program, Volume III, Supplement 1—Prediction Methods," Tech. Rep. FAA-RD-74-125 III-I (AD A030376), FAA, 1976.

[10] Ho, P. Y., and Doyle, V. L., "Combustion Noise Prediction Update," AIAA Paper 1979-0588, 5th AIAA Aerocoustics Conference, Seattle, Washington, 1979.

[11] Hough, J. W., and Weir, D. S., "Small Engine Technology (SET)—Task 13 ANOPP Noise Prediction for Small Engines: Jet, Core, and Turbine Module Revisions," Tech. Rep. No. 21-9655, AlliedSignal Engines, Phoenix, Arizona, 1997.

[12] Mathews, D. C., Rekos, Jr, N. F., and Nagel, R. T., "Combustion Noise Investigation," Tech. Rep. FAA-RD-77-3, FAA, 1977.

[13] Mathews, D. C., and Rekos, Jr, N. F., "Prediction and Measurement of Direct Combustion Noise in Turbopropulsion Systems," *J. Aircraft*, Vol. 14, No. 9, 1977, pp. 850–859.

[e] K. M. Tacina, private communication 2015

[14] Mahan, R. J., and Karchmer, A., "Combustion and Core Noise," *Aeroacoustics of Flight Vehicles: Theory and Practice*, Vol. 1, edited by H. H. Hubbard, NASA Reference Publication 1258, WRDC Technical Report 90-3052, 1991, Chap. 9, pp. 483–517.

[15] Hultgren, L. S., "Full-Scale Turbofan-Engine Turbine-Transfer Function Determination Using Three Internal Sensors," AIAA Paper 2011-2912 (NASA/TM-2012-217252), 17th AIAA/CEAS Aeroacoustic Conference, Portland, Oregon, 2011.

[16] Hultgren, L. S., "A Comparison of Combustor-Noise Models," AIAA Paper 2012-2087 (NASA/TM-2012-217671), 18th AIAA/CEAS Aerocoustics Conference, Colorado Springs, Colorado, 2012.

[17] Schuster, B., and Lieber, L., "Narrowband Model for Gas Turbine Engine Combustion Noise Prediction," AIAA Paper 2006-2677, 12th AIAA/CEAS Aerocoustics Conference, Cambridge, Massachusetts, 2006.

[18] Motsinger, R., "Prediction of Engine Combustor Noise and Correlation with T64 Engine Low Frequency Noise," Tech. Rep. R72AEG313, General Electric Co., 1972.

[19] Weir, D. S., "Engine Validation of Noise and Emission Reduction Technology Phase I," Tech. Rep. NASA/CR-2008-215225, NASA, 2008. Honeywell Report No. 21-13843, Honeywell Aerospace, Phoenix, Arizona.

[20] Miles, J. H., "Aligned and Unaligned Coherence: A New Diagnostic Tool," AIAA Paper 2006-0010 (NASA/TM-2006-214112), 44th Aerospace Sciences Meeting, Reno, Nevada, 2006.

[21] Miles, J. H., and Hultgren, L. S., "Application of an Aligned and Unaligned Signal Processing technique to Investigate Tones and Broadband Noise in Fan and Contra-Rotating Open Rotor Acoustic Spectra," Tech. Rep. NASA/TM–2015-218865 (ISABE-2015-20243), NASA, 2015.

[22] Sree, D., "A Novel Signal Processing Technique for Separating Tonal and Broadband Noise Components from Counter-Rotating Open-Rotor Acoustic Data," *International J. Aeroacoustics*, Vol. 12, No. 1+2, 2013, pp. 169–188.

[23] Sree, D., and Stephens, D. B., "Tone and Broadband Noise Separation from Acoustic Data of a Scale-Model Contra-Rotating Open Rotor," AIAA Paper 2014-2744, 20th AIAA/CEAS Aeroacoustics Conference, Atlanta, Georgia, 2014. doi:10.2514/6.2014-2744.

[24] Davis, I., and Bennett, G. J., "Spatial Noise Source Identification of Tonal Noise in Turbomachinery Using the Coherence Function on a Modal Basis," AIAA Paper 2011-2825, 17th AIAA/CEAS Aeroacoustic Conference, Portland, Oregon, 2011.

[25] *Handbook of Aviation Fuel Properties*, 3rd ed., CRC Report 635 (AFRL-PR-WP-TR-2004-2127). Coordinating Research Council, Inc., 2004. URL `http://www.dtic.mil/dtic/tr/fulltext/u2/a429439.pdf`.

[26] Mattingly, J. D., *Elements of Propulsion Gas Turbines and Rockets*, AIAA, 2006.

[27] Van Wylen, G. J., and Sonntag, R. E., *Fundamentals of Classical Thermodynamics, SI Version*, second (revised printing) ed., Wiley, 1978.

[28] *NIST Chemistry WebBook, SRD 69*, National Institute of Standards and Technology, 2017. URL `https://webbook.nist.gov/chemistry/`.